APPLIED PHYSICS

Deep learning for enhanced spectral analysis of MA-XRF datasets of paintings

Zdenek Preisler[1]*, Rosario Andolina[1], Andrea Busacca[1], Claudia Caliri[1,2], Costanza Miliani[1], Francesco P. Romano[1,2]*

Recent advancements of noninvasive imaging techniques applied for the study and conservation of paintings have driven a rapid development of cutting-edge computational methods. Macro x-ray fluorescence (MA-XRF), a well-established tool in this domain, generates complex and voluminous datasets that pose analytical challenges. To address this, we have incorporated machine learning strategies specifically designed for the analysis as they allow for identification of nontrivial dependencies and classification within these high-dimensional data, thereby promising comprehensive interrogation. We introduce a deep learning algorithm trained on a synthetic dataset that allows for fast and accurate analysis of the XRF spectra in MA-XRF datasets. This approach successfully overcomes the limitations commonly associated with traditional deconvolution methods. Applying this methodology to a painting by Raphael, we demonstrate that our model not only achieves superior accuracy in quantifying the fluorescence line intensities but also effectively eliminates the artifacts typically observed in elemental maps generated through conventional analysis methods.

INTRODUCTION

In the past decade, the use of imaging techniques for the noninvasive investigation of paintings has seen rapid progress. Their capabilities have been demonstrated in various applications focused on pigment identification, pigment degradation, virtual restoration, and technical art history (*1*–*8*). However, each of these techniques produces large datasets, and the analysis requires specific scientific expertise, as well as a solid knowledge of instruments and measurement conditions used. It is therefore natural that the availability of these complex data has driven in parallel new developments of elaborate analytical procedures and computational methods. More recently, the heritage science domain has benefited from cutting-edge artificial intelligence algorithms used for addressing challenging tasks and for finding out insights that can go unnoticed using classical analysis (*9*–*13*). Macro x-ray fluorescence (MA-XRF) is a well-established noninvasive technique becoming routinely used in museums and conservation studios for painting investigation (*14*–*18*).

It is performed by scanning the painted surface providing elemental distribution images that are relevant for pigment identification and to better elucidate the painting technique and the creative process of the artist. The MA-XRF scan collects XRF spectra across the surface of the object generating a large amount of data. The output is a three-dimensional (3D) data cube with a total number of pixels over the scanned area that can be on the scale of megapixel, i.e., millions of XRF spectra. This commonly happens when the measurement is operated on large artworks or when it is performed at high lateral resolution, often available in devices where the primary radiation is focused down to the micrometric scale with x-ray optics. It is evident that a manual analysis of such a large amount of XRF spectra is not feasible, and batch procedures have been elaborated overtime to approach this task (*19*–*21*).

A typical analysis of a MA-XRF data cube consists of using deconvolution algorithms that, through a minimization procedure, estimate the number of net counts per selected elemental fluorescence lines presented in each XRF pixel spectrum. The analysis is run by using average models prepared a priori that describes the experimental setup used and the assumed elemental composition of the investigated sample. This latter information is generally extracted at the end of the scan from the integral XRF spectrum of the full dataset. However, the rules governing the XRF spectra are complex with several nontrivial effects that depend on both the experimental conditions and on the chemical composition and structure of the sample. This means that shape and intensity of the spectrum, background, signal-to-noise ratio, and the presence of scattering and diffraction peaks can be different pixel by pixel. In addition, even the calculation of concentrations of pure elements (e.g., pictorial layers with a specific pigment) is strenuous due to the complex physics at play involving the unknown sample stratigraphy and composition. As a result, both the data processing and data interpretation pose a challenge ordinarily requiring an expert in the field to perform the analysis as accurately as possible.

In recent years, this has led to a plethora of novel computational methods aimed at automating and assisting MA-XRF analysis or the XRF analysis in general. In particular, the application of unsupervised machine learning algorithms has been attempted to improve data interpretation. This often leads to clustering methods such as *K*-means, principal components analysis, non-negative matrix factorization, unified manifold approximation and projection, self-organizing maps, t-distributed stochastic neighbor embedding (t-SNE), and their various modifications (*12*, *22*–*26*). While these approaches are useful, they are still not without drawbacks. A particular challenge is to interpret their outputs and assign them a physical meaning.

An alternative is to use supervised machine learning, where one trains an artificial intelligence network using labeled XRF spectra. To our best knowledge, this has been used only to train convolutional neural network (CNN) classifiers where one attempts to predict whether a specific pigment is present in the spectra. One

[1]CNR, Istituto di Scienze del Patrimonio Culturale, Via Biblioteca 4, 95124 Catania, Italy. [2]INFN, Laboratori Nazionali del Sud, Via Santa Sofia 62, 95123 Catania, Italy.
*Corresponding author. Email: zdenek.preisler@cnr.it (Z.P.); francescopaolo.romano@cnr.it (F.P.R.)

example is the work by Jones *et al.* (*27*) and another work is by Xu *et al.* (*28*). In both cases, they used a fundamental parameters approach to generate synthetic spectra used for training. In the second case, they also include experimental spectra from a mockup. We, however, believe that the classification task to identify pigments from XRF spectra itself is an ill-defined problem. In general, without additional information coming from complementary molecular techniques and assumptions on stratigraphy and composition, it is particularly challenging to distinguish and identify pigments containing the same elements from the XRF spectra alone.

Here, we introduce a deep learning model, trained using synthetic spectra only, providing fast and accurate estimates of the elemental distribution maps. The model is trained using more than 500,000 synthetic spectra generated by Monte Carlo (MC) simulations (*29*). Our simulations assume a five-layer physical model describing the painting's structure (see Fig. 1A). The simulation configuration is set to match our instrumental setup as closely as possible to maximize the fidelity of the spectra (see Fig. 2). Notably, with the use of our trained model, we recover not only the correct elemental distributions of paintings but also the absolute number of counts for each chemical element in the XRF spectra by introducing scale in the neural network. Hence, we present it as an alternative to classical deconvolution analysis substantially reducing the time for the analysis and the expertise needed. We demonstrate that the use of our trained network is robust enough to provide reliable results of complex pictorial contexts. We show that, in some cases, the model even yields superior quality results and helps to avoid artifacts present in elemental distribution images calculated using traditional deconvolution.

As a pilot study for this research, we apply the new methodology to two paintings by Raphael in exhibition at the Museo di Capodimonte (Napoli, Italy). The paintings considered here, *God the Father* (wood panel, 110 cm by 73 cm), and *Virgin Mary* (wood panel, 51 cm by 41 cm), represent two of only four preserved fragments of a grand altarpiece painted by Raphael in 1500–1501 (see fig. S1). MA-XRF data were recorded in situ in several scanning sessions with different lateral resolutions ranging from the millimetric to the micrometric scale by using our custom-developed MA-XRF system (*15*, *30*).

RESULTS

We apply the neural network model to the MA-XRF datasets from the two panel paintings by Raphael. In addition, we perform a

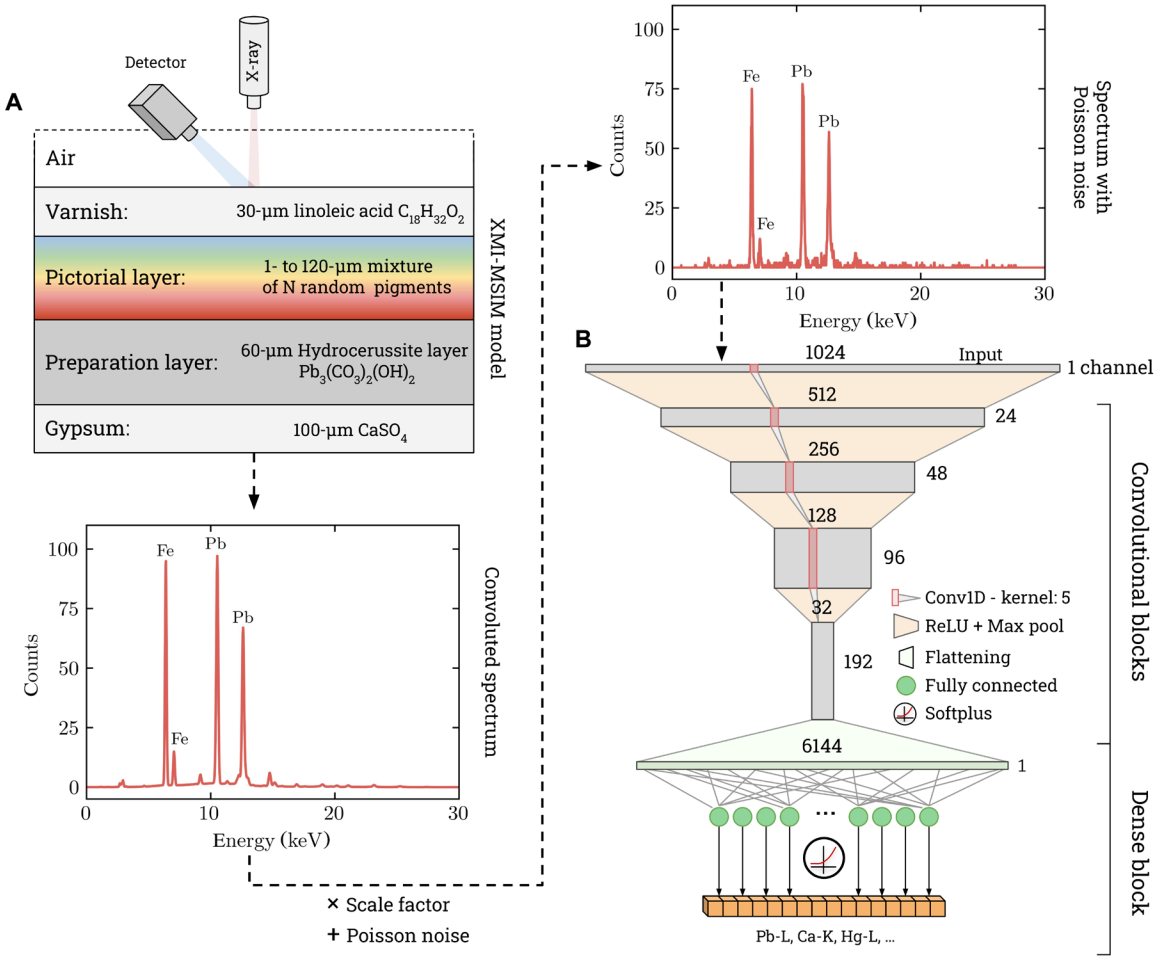

Fig. 1. Schematics of the proposed approach. (**A**) Schematics of the pictorial model used in the MC simulation to generate the synthetic XRF spectra for training the network. (**B**) Schematics of the neural network used here. We divide the network into two parts: the convolutional blocks and the dense block. The dense block is kept fixed in the first part of training and is enabled only after the convolutional blocks are trained. ReLU, rectified linear unit.

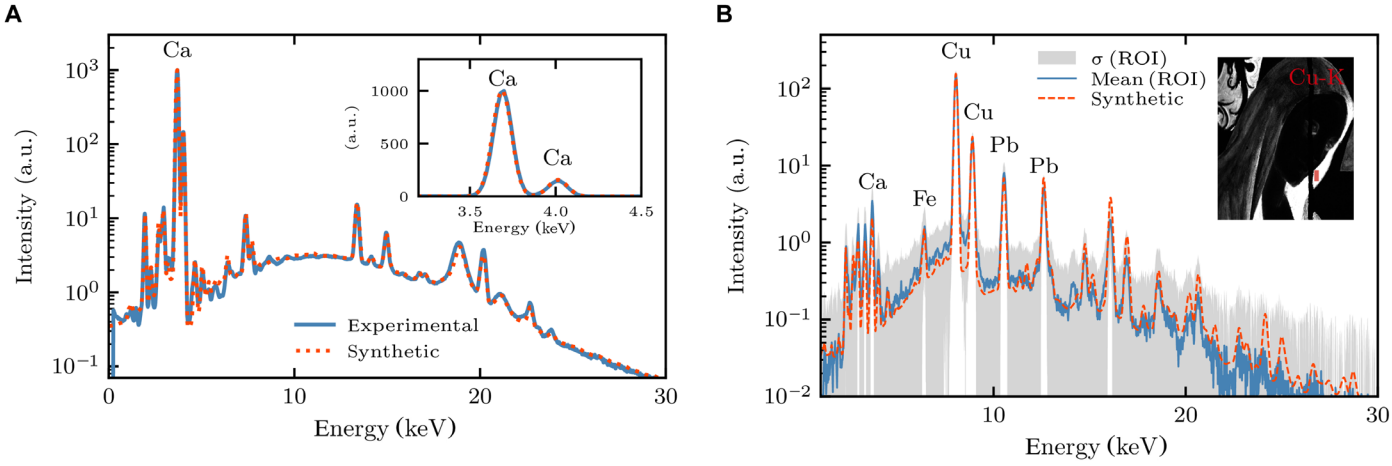

Fig. 2. Synthetic spectra. (**A**) Simulated spectrum of calcite. The graph shows our ability to simulate a spectrum of a known sample. The geometry used in the simulation is the same as the one used to build the synthetic dataset. (**B**) Simulated spectrum of a group of pixels taken from a specific region in the *Virgin Mary* panel dataset. The red dashed line corresponds to the spectrum simulated using the same model and the setting as the spectra in the synthetic dataset. The concentrations of the detected elements are found numerically and used in the simulation to define the painting model. The blue line is an average spectrum over a ROI indicated by the red rectangle in the image. The gray area indicates the SD of the experimental spectra selected. a.u., arbitrary unit.

comparative analysis with classical deconvolution algorithms to further establish the validity of the model's results. As will be elaborated further below, our approach involves training of the neural network with a synthetic dataset mimicking a generic painting with a hydrocerussite preparation layer. This is a step forward in the ability to perform the MA-XRF analysis because it eliminates the needs for a priori assumption about the elemental composition as necessary in the classical analysis. Instead, we use a general list of pigments with a simple stratigraphy model to describe the painting and run the simulations to generate the synthetic training dataset. Besides the historical pigments used during the 15th century, we also include anachronistic pigments as they are often detected by the MA-XRF scans in repainted areas and restorations. Together, 57 pigments and compounds are used to generate the synthetic dataset (see table S1).

We show not only that it is possible to train the network using only the synthetic dataset but also that we can obtain state-of-the art performances using this methodology in analyzing complex pictorial contexts. To demonstrate the accuracy and applicability of our approach, we compare the elemental distribution maps calculated using traditional deconvolutional algorithms and our neural network predictions. In this research, the classical analysis of the MA-XRF datasets was done using the open-source software PyMCA (*19*). In the following, we refer to this analysis as a reference for the purpose of comparing and validating our results.

AI/ML maps of the two panel paintings

In our study, we analyzed four datasets from two panel paintings by Raphael. This included two MA-XRF scanning datasets covering the entire panel paintings, conducted with a step size of 1 mm, alongside two high-resolution scans focusing on selected areas of interest in the pictorial composition. These scans were executed at a step size of 250 μm for *God the Father* panel and a step size of 50 μm for the *Virgin Mary*.

The resulting MA-XRF elemental distribution images, obtained from both traditional analysis and artificial intelligence/machine learning (AI/ML) methodology, are compiled in figs. S2 and S3 for the full paintings and fig. S4 for the high-resolution datasets. Across all datasets, the congruence between reference images and AI/ML-generated elemental distributions is notable, validating the efficacy of neural network predictions as an alternative option to the classical MA-XRF analysis in the examination of painted artworks. The pigment palette inferred from the neural network aligns with 15th century practices and matches the one used by Raphael in its early work (*31*–*33*). Notice that MA-XRF is an elemental technique, and it should be combined with other analytical techniques to elucidate pigment-specific information. In addition, x-rays that have penetrating power and information provided by the elemental distribution images are integrated over the pictorial layer.

Key findings that can be deduced from the elemental distribution images include the use of lead white in preparatory layer and highlights, red vermillion in skin tones and chiaroscuro enhancements, copper green in draperies, and iron and manganese oxides in depicting the two figures and the other elements of the pictorial composition in of the background. The copper green is associated with potassium, suggesting the use of a copper resinate or the use of azurite mixed with a yellow organic lake. The blue pigment is also characterized by the presence of copper (suggesting the use of azurite) layered with lapis lazuli (or with a lake) mixed with lead white, as can be deduced from the potassium and lead distribution maps (*34*). Some key elemental distribution images are presented in Fig. 3 for the panel "*Virgin Mary*," showcasing the distribution of lead (Fig. 3B), mercury (Fig. 3C), gold (Fig. 3D), copper (Fig. 3E), and iron (Fig. 3F).

The MA-XRF scans also revealed the gilded motifs of the two panel paintings, partially obscured in the current visible pictorial composition, and detected restorative work occurred over time involving anachronistic pigments. Figures 4 and 5 offer a high-resolution view of relevant elemental distributions in selected areas of *God the Father* and *Virgin Mary*, respectively. These images shed light on Raphael's early pictorial techniques. Notably, the correlation map in Fig. 4D, with color components red (Hg-L), green (Fe-K), and blue (Cu-K), elucidates the use of the subtle modeling technique in the

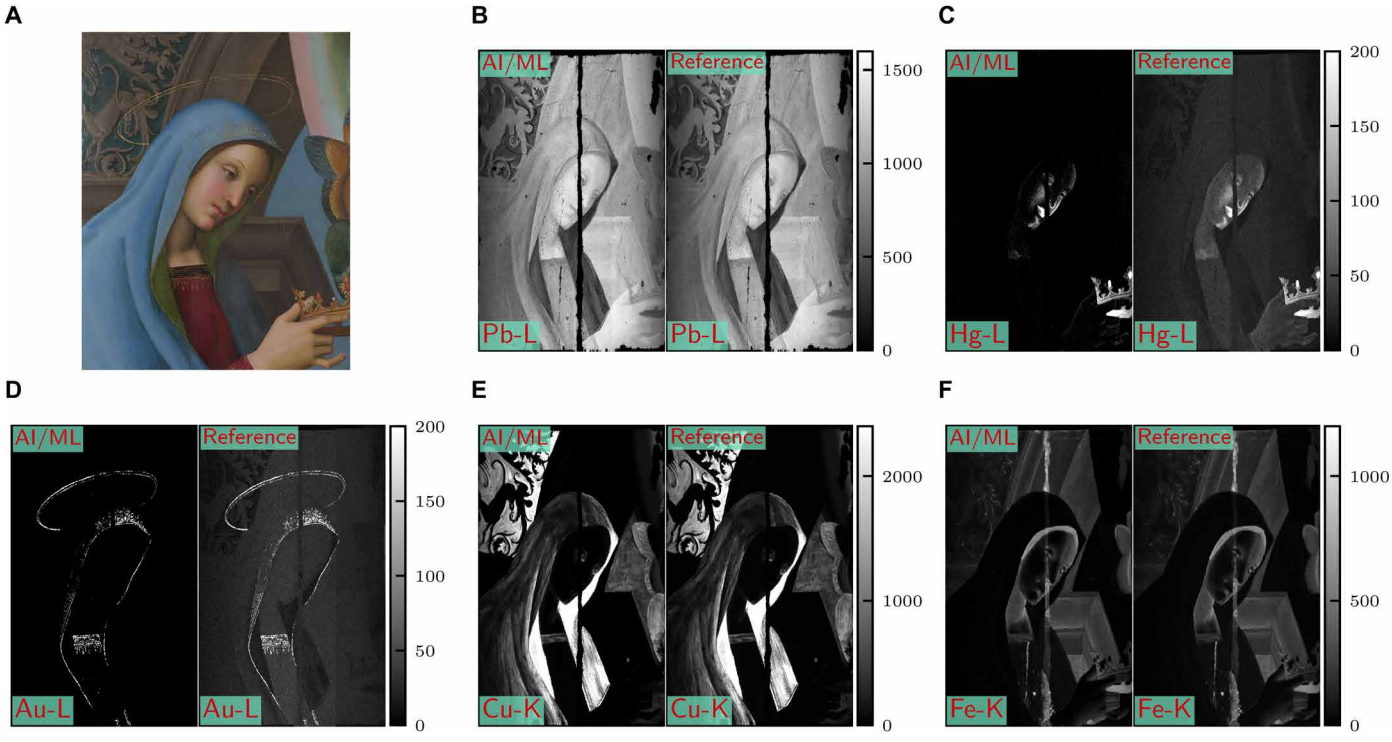

Fig. 3. Elemental distribution maps of MA-XRF of the *Virgin Mary*. In all cases, we display the AI/ML predictions on the left and the reference estimates on the right. (**A**) Visible image of the scanned area. (**B**) Elemental maps of Pb-L. The maps match very closely. (**C**) Elemental map of the Hg-L shows that the reference net counts are higher for the low net counts, especially in the presence of Pb-L. This is particularly pronounced in the facial features and the hand. This effect is an artifact of the deconvolution procedure. (**D**) Elemental counts of Au-L show the background noise produced by the deconvolution in the reference map on the right. The network, on the other hand, is much less susceptible to this. (**E**) Elemental distribution maps of Cu-K. (**F**) Elemental distribution maps of Fe-K. These match the net intensity inferred very closely. [Credits: Photo (A) by Danilo Pavone, ISPC-CNR, Catania]

facial painting, leaving the lead white preparation exposed (not visible in the figure) and using ochres to impart three-dimensionality and shadowing while red vermillion with a layer of a Cu-based pigment around the eyes to create nuanced skin tones. The high-resolution maps in Fig. 5B provide insights into Raphael's underdrawing techniques, especially evident with the use of a lead tip for delimiting the architectural details.

A notable correlation between iron and zinc, visible in Fig. 5 (C to E), points to the origin of the ochre used by Raphael (*35*). We used MC simulations to model this area of the painting and extract XRF spectra matching our experimental data. We estimate the average weight ratio of ZnO to Fe_2O_3 to be 0.12 ± 0.03, aligning with previous estimates for this specific pigment (*35*). This average value is calculated over eights regions of interest (ROIs) indicated in fig. S5B.

Comparative analysis of AI/ML predictions versus the deconvolution analysis

For the elemental lines with mid and high net counts such as Pb-L, Cu-K, and Fe-K, the results obtained from the AI/ML model and the classical deconvolution method are mostly indistinguishable without a statistical/quantitative analysis. The most notable differences are visible where the elemental line counts are low, i.e., low signal-to-noise ratio. We find that deconvolutional analysis has a slight tendency to overestimate the counts in these instances, including cases when the element is not present. Consider, for example, the elemental map of Au-L in Fig. 3D. The Au-L low counts detected in the reference map in the background are an artifact because there is no gold present.

The network provides superior results in this case as there are no false-positive net counts. In the case of Hg-L, the classical deconvolution tends to detect mercury even if it is not present (see Fig. 3C) or to overestimate its counts in the simultaneous presence of lead in the flesh tones. Differences can also be seen when evaluating separate maps of the Hg-L series. For example, the Hg-L_1 reference map is expected to be problematic by default as it includes line energies below and above the Pb-L_3 edge, and the continuum background in the experimental spectrum is not properly elaborated by the deconvolution fitting procedure. We see this in the elemental maps of Hg-L_1 and Hg-L_3 in Fig. 6 (A and B), where in the case of Hg-L_1, the Pb contribution makes the image noisier. On the other hand, the Hg-L_3 line reference estimate and the model prediction correspond to each other. The difference between the reference and our estimate for Hg-L_3 lines is shown in Fig. 6C.

Another pair of interests are iron and manganese. The Fe-Kα and Mn-Kβ emission lines are very close in energy, 6.40 and 6.49 keV respectively, which renders their estimate more problematic compared to the other elements. Mn-Kα has an energy of 5.90 keV, and Fe-Kβ has an energy of 7.06 keV. The proposed AI/ML model can separate the contributions of both elements more precisely, hence providing an improved estimate of counts. In the case of the *Virgin Mary* (see Fig. 5), we estimate less than 1 count of Mn-K per pixel,

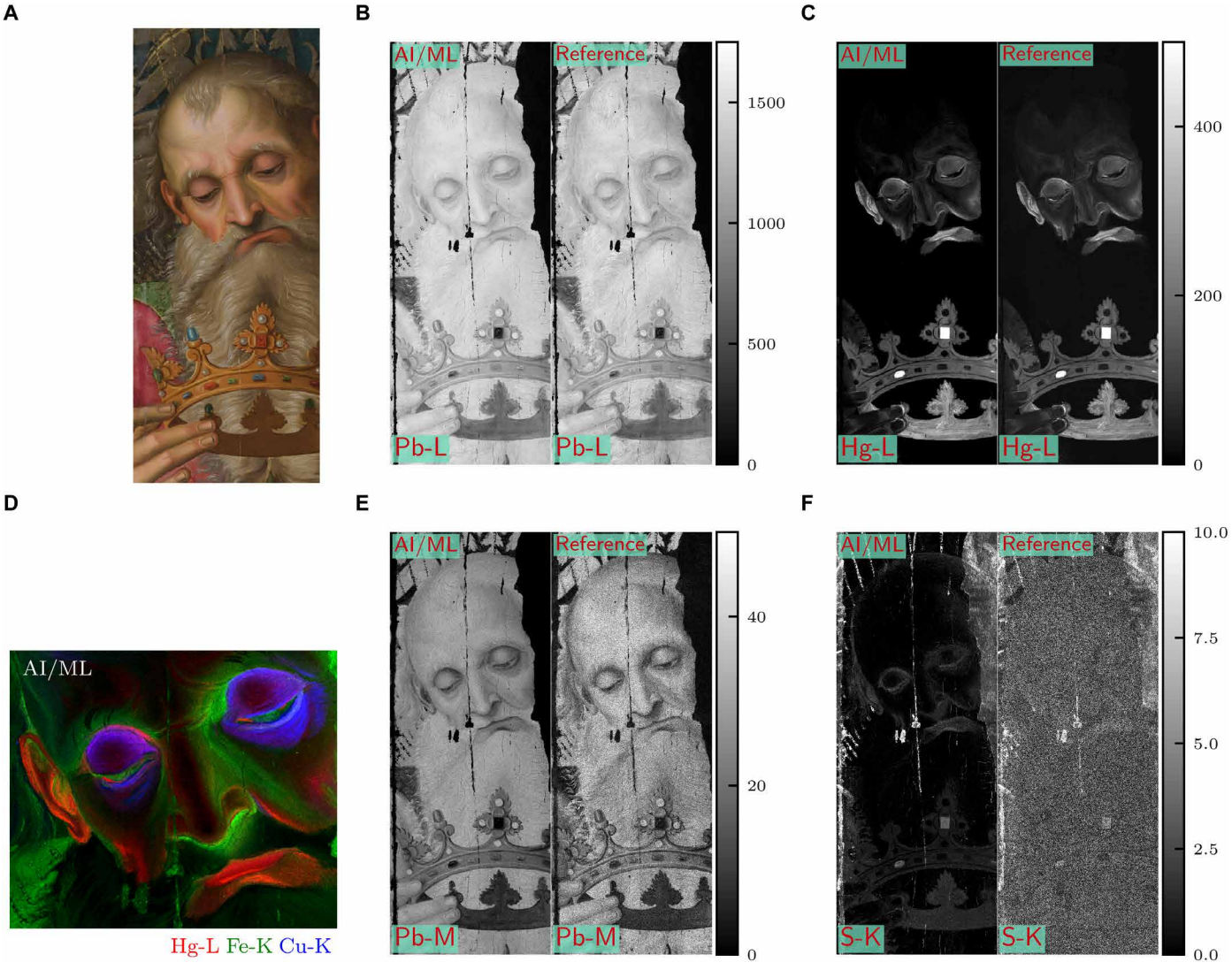

Fig. 4. High-resolution MA-XRF elemental distribution maps of the detail of *God the Father*. (**A**) Visible image of the scanned area. (**B**) Elemental map of Pb-L. (**C**) Elemental maps of the Hg-L. (**D**) Composed Red-Green-Blue (RGB) image of the elemental distribution maps of Hg-L, Fe-K, and Cu-K. The image provides insight into the painting technique of Raphael. (**E**) The elemental distribution maps of Pb-M. The AI/ML estimates are lower than the ones of the reference. The network, however, provides a less noisy output. (**F**) Elemental distribution maps of S-K. The AI/ML image is predicted, while the reference, due to the low net counts of sulfur and the energy overlap of S-K with the Pb-M, is too noisy to be interpreted. [Credits: Photo (A) by Danilo Pavone, ISPC-CNR, Catania]

suggesting the accurate prediction of the network. On the contrary, the reference Mn-K is overestimated due to the Fe-K and the continuum contribution. The same occurs in the case of the manganese and iron distribution images in *God the Father* (see Fig. 6). We show the Mn-K image that contains Mn-Kβ that overlaps with Fe-Kα lines. To further elaborate, we display the Mn-Kα image only. In this case, the reference estimate is more appropriate and in better agreement with the network prediction. Here again, we estimate the average number of net counts of the Mn-K in a ROI obtaining 5 counts per pixel, which is below the reference estimate.

Besides the above examples, we can also separate the contributions from Pb-M and S-K (see Fig. 4, E and F). Not only are these lines close in energy, 2.31 and 2.46 keV for S-K and 2.35 keV for Pb-M, but also they are in a low-energy region where estimates are challenging due to low intensities and many elemental lines present (i.e., scattering L-lines peaks from the sources or other L lines from heavy elements). The S-K map is very noisy, while the AI/ML prediction shows the pictorial details (i.e., the sulfur in the red gemstone on the crown and the lips as expected from the use of red vermillion, confirmed in the Hg map). We set the same colormap for both the references and for our predictions, so a specific number of net counts correspond to the same color.

Apart from the above, we also provide a quantification of the results to demonstrate that we recover an absolute number of net counts for the elemental lines and not only their distribution. In Fig. 7, we show histograms and plots of AI/ML estimates versus the reference for each pixel for selected elements. The histograms provide information about how the counts are distributed in the

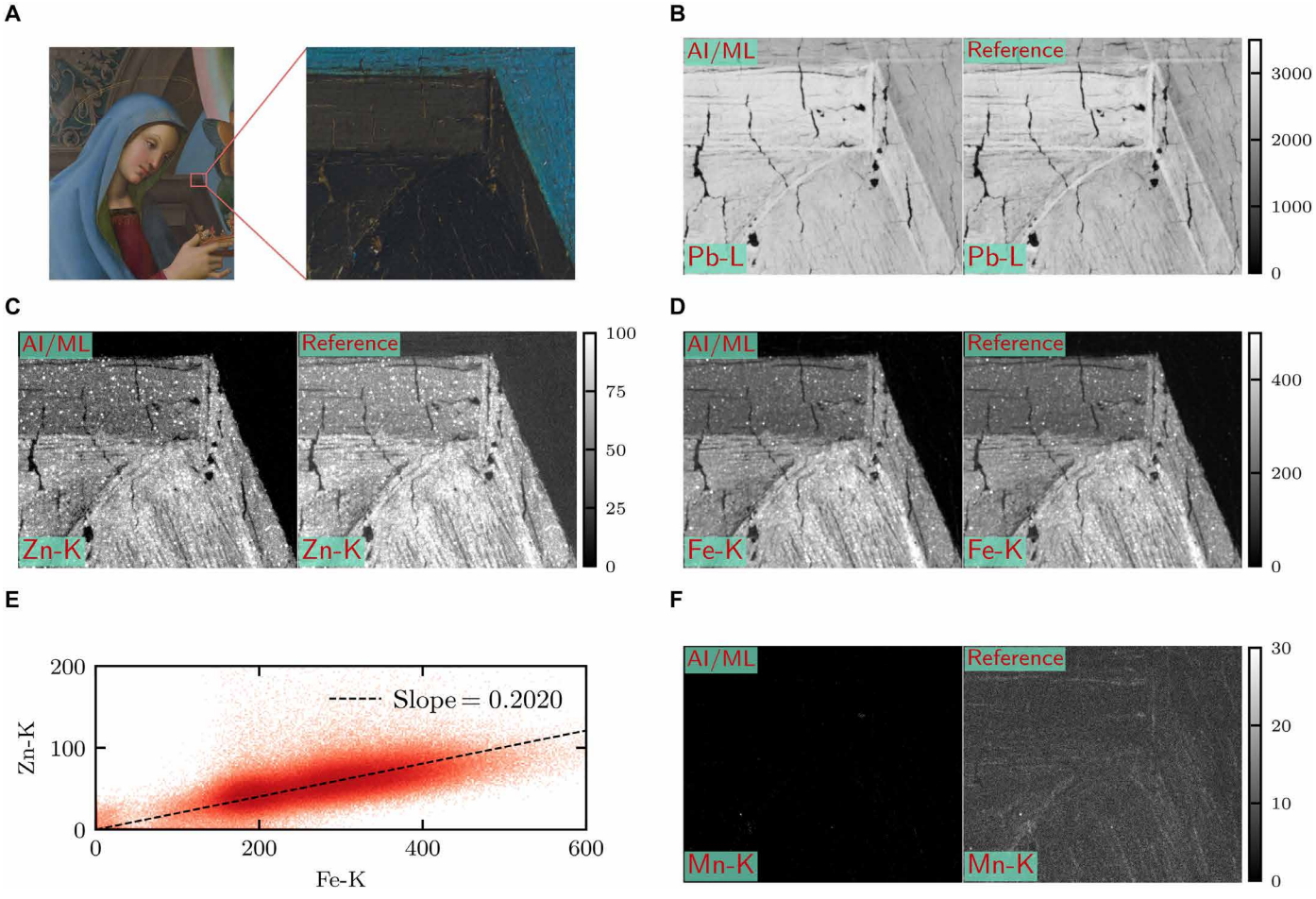

Fig. 5. High-resolution MA-XRF elemental distribution maps of the architectural detail in the painting of the *Virgin Mary*. (**A**) Visible image of the scanned area. (**B**) Elemental map of Pb-L. This image shows the lead tip used by Raphael in the preparation drawing. (**C**) Elemental distribution maps of Zn-K. (**D**) Elemental distribution map of Fe-K. (**E**) Correlation between Zn-K and the Fe-K indicates that the natural ochre used by Raphael is associated with a high concentration of zinc. (**F**) Elemental distribution map of Mn-K. The AI/ML prediction shows no signals. We find that the average number of net counts per pixel is less than 1. The counts detected in the reference are artifacts. [Credits: Photo (A) by Danilo Pavone, ISPC-CNR, Catania]

corresponding maps, where for identical predictions, the curves will overlap. In the case of experimental spectra, the actual net counts of the elemental lines, i.e., the ground truth, are not known. Hence, we use the reference estimate as a close approximation for the purposes of the evaluation of the model, although it can vary slightly depending on the settings of the fitting model used for the deconvolution.

We find that our predictions and the reference match very closely. In particular, the net counts follow the same distributions, and we recover the same scale for both estimates. The most notable differences are again in the low count regions. The reference displays a pillar as it tends to slightly overestimate when the element is not present, which follows the arguments presented above. In the case of the very high counts, we observe that the reference occasionally slightly underestimates with respect to the network estimates. To further quantify the results, we plot the reference versus the prediction for each pixel, where the same predictions correspond to the indicated dashed black line. All the graphs show good agreement with the reference. Again, the only exceptions are the low count backgrounds and the high counts, where the points drift above the black dashed line discussed above.

Figure of merit of the AI/ML model

To further evaluate the precision of the network and to provide more insight, we build an additional synthetic dataset using lead white as preparatory layer and a mixture of two pigments mixed with a binder as pictorial layer: vermilion, HgS, and lead white $[Pb_3(CO_3)_2(OH)_2]$ (see Fig. 8A). The volume fraction of the binder is fixed at 50%, and we vary the mass fraction of the lead white and vermilion (see fig. S7). Because the dataset is synthetic, we have the exact labels associated with each simulated spectrum, which in turn allows us to better estimate the errors of both the AI/ML model and the reference deconvolution method. To populate the dataset, we vary the vermilion mass fraction on the logarithmic scale, and we generate 1000 spectra for each data point to compute a mean and an SD for our estimates. We analyze this dataset by both our AI/ML model and the deconvolution procedure estimating the fluorescence lines net counts. To obtain better fit results when performing the

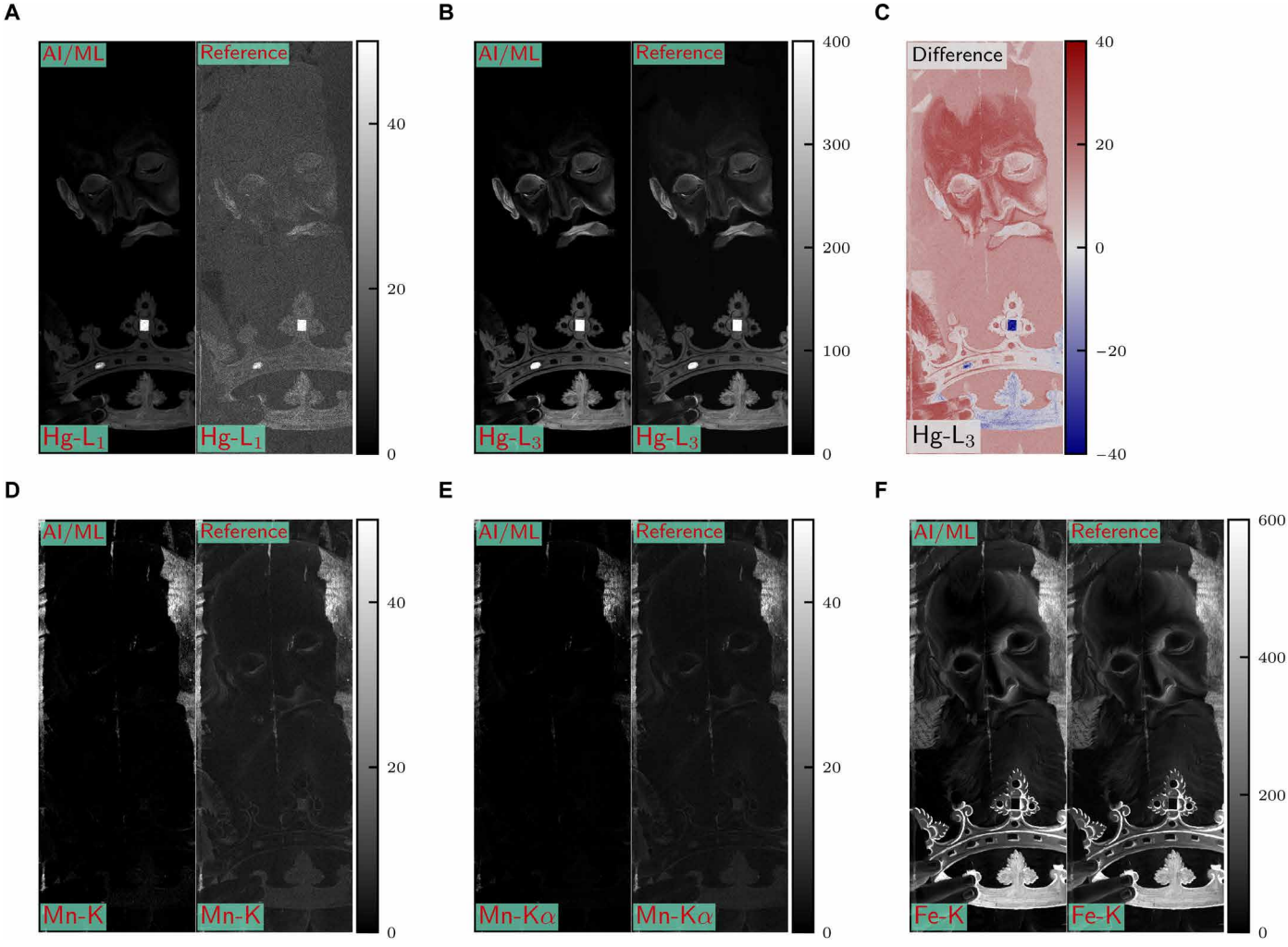

Fig. 6. High-resolution MA-XRF elemental distribution maps of the detail of the *God the Father* for separate lines of Hg. (**A**) Elemental maps of Hg-L_1. (**B**) Elemental map of Hg-L_3. (**C**) Difference between the elemental maps of the Hg-L_3 for the reference and our model. (**D**) Elemental map of Mn-K. (**E**) Elemental map of Mn-Kα. This elemental line does not overlap with the Fe-Kα, which results in the mismatch between the AI/ML model prediction and the reference. (**F**) Elemental map of Fe-K.

deconvolution, the fitting model includes the characterization of the x-ray source of our MA-XRF setup, the geometry, and the matrix composition as defined in the simulation generating the synthetic dataset.

The outcome of this analysis is aligned with the findings described above. Despite the fine-tuned setting, the deconvolution approach slightly undervalues the Pb-L, while the neural network model recovers the simulation values (see Fig. 8B). Figure 7C shows that the deconvolution fits the Hg-L lines even in the absence of mercury when lead is present; hence, it gives false-positive counts. This agrees with our observations in the elemental maps. The neural network accurately estimates Hg-L down to 70 net counts. Below this number, it will underestimate. Both the network and the deconvolution estimate average S-K counts well (see Fig. 8F). However, the deconvolution has a larger SD, meaning that estimate is noisier. This corresponds to our findings as well when evaluating the elemental distribution maps (see Fig. 5). The network slightly underestimates the net counts of Pb-M compared to the deconvolution, but at the same time, the SD is smaller, resulting in less noisy maps. This again reflects our observation when analyzing the elemental distribution images of the two panel paintings.

In addition to the above, we evaluate the same synthetic dataset using the deconvolution with the fitting model corresponding to the one used for the painting where many elements are included in the fitting procedure. In Fig. 8E, we show estimates for As-K and Au-L. In both cases, the deconvolution shows false counts. This is unavoidable for paintings where many pigments are present and a general fitting configuration model including many elemental lines is necessary. The As-K lines are close in energy to Pb-L lines, and hence, the fitting procedure tends to assign counts to As-K when Pb-L is present. The network, however, in both cases provides an appropriate estimate.

DISCUSSION

The primary achievement of this study lies in the effective implementation of a neural network model for the analysis of MA-XRF datasets obtained from complex pictorial contexts. It marks a

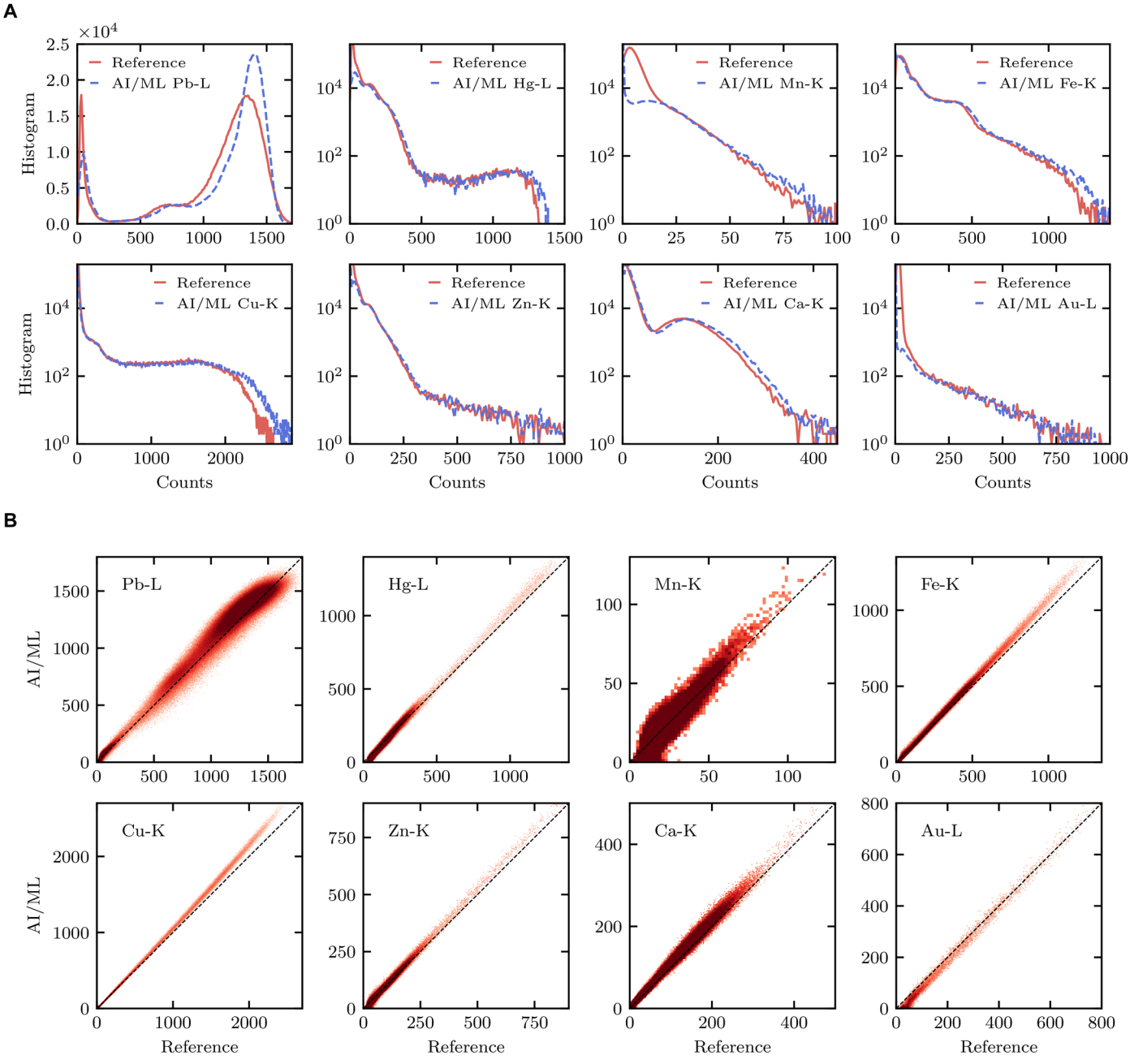

Fig. 7. Comparisons of the elemental distribution maps. (**A**) Histograms of the net counts for selected elements. The histograms of the Pb-L are shown on the linear scale, while the rest are shown on the logarithm scale for clarity. The graphs show that both the AI/ML and the reference recover the net counts on comparable scales. The histograms indicate that the reference predicts slightly lower net count at high intensities. On the other hand, at the very low counts, the reference overestimates, creating a pillar which in the images corresponds to the background noise. (**B**) Plots of AI/ML estimates versus the reference for each pixel for selected elements. Identical results lie on the black dashed line. The color gradient is a guide for the eye, where the darker red indicates more points present. The graphs show that both approaches generate closely matching results, and the combined estimates follow the black dashed line very tightly.

notable advancement in processing the XRF spectra, yielding elemental distribution images from MA-XRF scans of enhanced accuracy. The AI/ML model of this study effectively overcomes the limitations and artifacts commonly associated with traditional deconvolution analysis methods. Quantitatively, we have proven its capability in precisely predicting the absolute number of net counts for each elemental line analyzed. A noteworthy aspect of the model's performance is its superior accuracy in scenarios with low net counts, a situation where the traditional analytical methods typically tend to overestimate. Furthermore, the CNN model adeptly manages the identification and separation of closely overlapping fluorescence lines within the XRF spectra, and it is currently one of

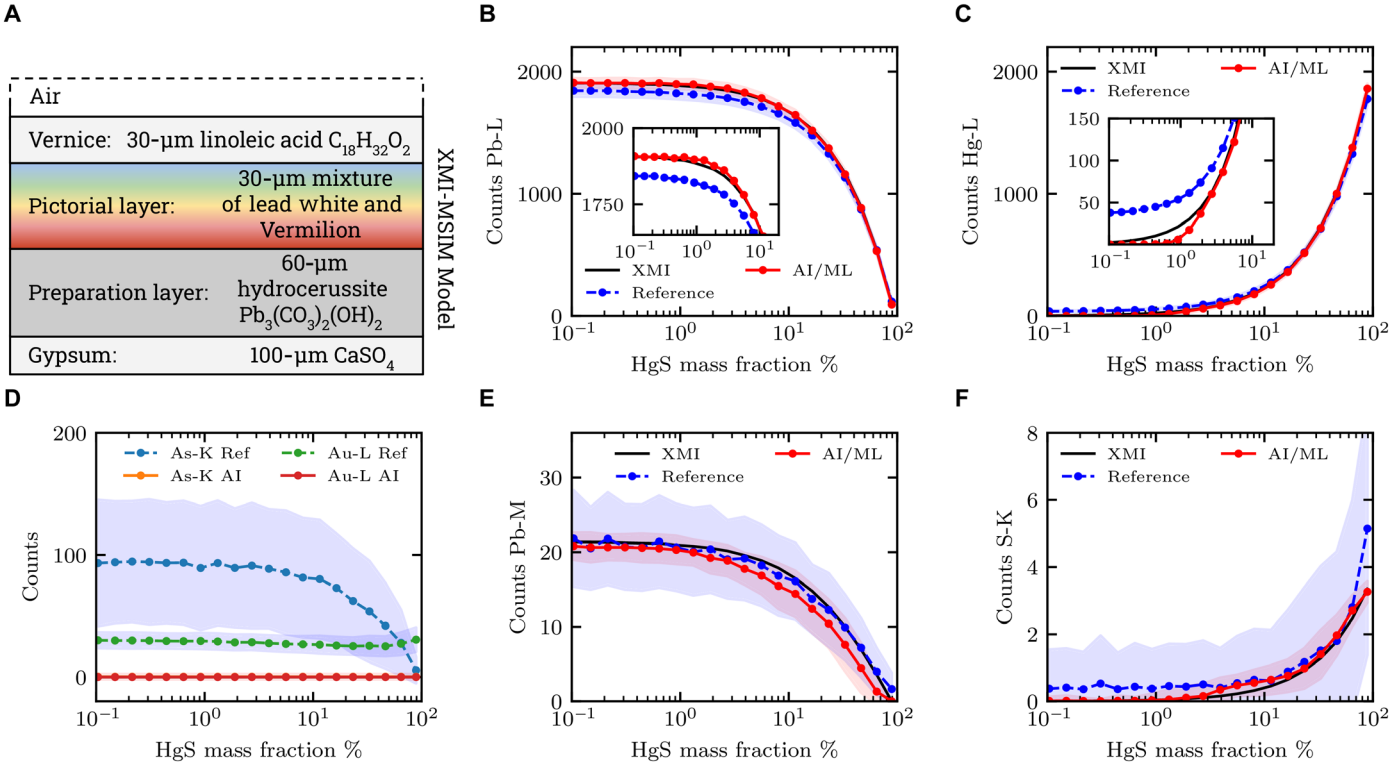

Fig. 8. Quantification of accuracy using a known synthetic dataset. (**A**) Composition of the synthetic dataset. We use the same stratigraphy model as the one used for the painting except for the pictorial layer, which is a mixture of lead white, vermilion, and binder. The volume fraction of oil is fixed, and we vary the mass fraction of the lead white and vermilion (**B**) Predicted net counts of Pb-L. The red lines correspond to our prediction, while the blue lines denote the reference estimates. The shaded regions indicate the SDs, respectively. The black line indicates the XMI counts, i.e., the ground truth. (**C**) Predicted net counts of Hg-L. The inlet shows that the neural network follows the ground truth to around 70 counts, after which it predicts zero. (**D**) Here, we perform the reference analysis using additional elemental lines not present in the sample. The graph shows that the reference fits the elemental lines even in their absence. The network is much less susceptible to this, not resulting in false-positive net counts. (**E**) Prediction for the net counts of Pb-M. The network underestimates the counts more compared to the reference. The reference, however, has a higher SD, resulting in noisier images. (**F**) Predictions for the net counts of S-K. Both the network and the reference provide appropriate estimates. Here too, the network exhibits a lower SD compared to the reference.

the most effective methods for the precise analysis of interfering characteristic x-ray peaks. This capability is crucial for accurately estimating the distribution of the chemical elements, i.e., of the pigment materials in the painting, improving the interpretation of the results and, in turn, the knowledge of the artist's materials and technique. We have demonstrated that it is possible to train our neural network model using solely synthetic XRF spectra and to analyze extensive datasets of experimental spectra effectively without the need of any a priori assumption of the elemental composition. Furthermore, the construction of specific synthetic datasets provided a controlled environment to test the model's precision and to understand its detection limits and response variability across different pigment compositions and painting stratigraphy.

These findings represent a pivotal advancement in the integration of artificial intelligence for more accurate and efficient analysis of XRF spectra. This is particularly relevant for handling large datasets, such as those produced by MA-XRF imaging techniques commonly used in Heritage Science and thus further fostering interdisciplinary collaboration among the experts from various scientific disciplines in the field. The success of our approach is founded on two key pillars. First, the existed knowledge in the description of x-rays generation and interactions with matter, including the spectral responses of energy dispersive detectors, and second, the availability of advanced simulation software capable of generating synthetic spectra that closely emulate those obtained by XRF instruments. While in the present study we have demonstrated the application of this methodology related to a specific XRF spectrometer and the set of analyzed materials, its applicability can be easily extended.

In principle, we can generate large datasets of synthetic spectra within short timeframes, facilitating the production of reliable analytical results. This capability not only allows for the simulation of additional spectra but also enables the preservation of all simulation settings and parameters. These parameters, some unattainable through experimental methods, can be inferred, giving way to future extensions going beyond what is possible with conventional approaches. One can, for example, extend the methodology to attempt to infer a model stratigraphy or to estimate a conversion of spectra obtained with different instrumentations to make the data directly comparable. Nevertheless, we consider the dependence of the synthetic dataset on the experimental setup parameters (including x-ray source, geometry, optics, detector, etc.), on the sample matrix composition and stratigraphy, as the main limitation of the proposed methodology. We expect that this constraint will be progressively mitigated with future developments.

MATERIALS AND METHODS

AI/ML model structure

The AI/ML model presented in this work is based on CNN architecture, and the network is trained to infer the number of net counts per each selected series of emission fluorescence lines in XRF spectra. Note that this differs from other until date reported works (*10*, *11*) where CNN is used as a classifier, and it presents its unique challenges. In the design of the neural network, we consider that measured counts are affected by Poisson noise, and hence, the measured spectra cannot be individually rescaled. Because our task is to estimate the absolute number of counts, certain commonly used operations for training CNNs are purposefully avoided. This includes normalization, batch normalization, and dropout; in addition, all the biases in all layers are disabled. We use the 1D convolution layers as they are a natural choice to represent the XRF peaks. We aim to train the network kernels that give rise to expected shapes and positions of peaks present in the spectra. This contrasts with a typical CNN classifier where one hopes to learn distinguishing features of various classes. In that sense, the methodology is more analogous to the standard deconvolution methods used in XRF analysis, where the peaks themselves are modeled using deep convolutional layers rather than using Gaussian distributions.

This is also reflected in the training of the network. A typical CNN is translationally invariant. This property comes from the dense layer at the end of the network that picks relevant features for the classification. In our case, the fluorescence lines are characterized by their energies, i.e., their position in the arrays, and hence, we want to prohibit translational invariance. To this end, the training is carried out in two stages. In the first stage, the training of the dense layers is partially disabled, and we allow the training of all dense layers only after the network learns to represent the shapes of the peaks. Further, we adjust the training to introduce changes of scale that respect the Poisson noise. In other words, we want the network to predict the counts across a few orders of magnitudes. The absolute number of counts scales with dwell time per pixel, current and voltage of the primary x-ray source, and total detection active area, which are all factors commonly adjusted based on the experimental needs. While it is not possible to rescale a single experimental spectrum, the same is not true for our simulated spectra (i.e., the ones used for generating the synthetic training dataset), which do not include the Poisson noise. This allows us to simply rescale, i.e., multiply by a scale factor, the convoluted spectra first and consequently apply the Poisson noise on-the-fly during training. This also increases the training dataset diversity as no spectrum is fed to the network twice during the process, reducing issues with overfitting. We use L1 loss function with Adam optimizer with a learning rate of 10^{-4} and the batch size of 512. The L1 loss is divided by the scale factor used for each spectrum during training to calculate the backpropagation, i.e., the ratio loss = L1(label, prediction)/scale factor. The scale factor is chosen randomly on-the-fly per each spectrum between 0.05 and 100. We use spectra in the energy range from 0 to 30 keV, and the spectra are resampled from 2048 bins to 1024 bins to lower the computational requirements and to speed up the training. The network we use is a CNN structured as follows (see Fig. 1):

1) The 1024 bins spectrum is multiplied by a scale factor, and the Poisson noise is added.

2) The first convolutional layer with 24 kernels with a kernel size of 5 is applied with a zero padding of 2, producing 24 × 1024 feature maps.

Max-pooling layer with a kernel size and a stride of 2 together with a rectified linear unit (ReLU) is applied generating 24 × 512 feature maps.

3) The second convolutional layer with 48 kernels and a zero padding of 2 is applied, producing 48 × 512 feature maps.

4) Another ReLU and Max-pooling layer with both a stride and kernel size of 2 are applied, generating 48 × 256 feature maps.

5) The third convolutional layer is applied with 96 kernels and a zero padding of 2, obtaining 96 × 256 feature maps.

6) Follows the third ReLU and Max-pooling layer with a stride and kernel size of 2, which produces 96 × 128 feature maps.

7) The fourth convolution layer with 192 kernels with a stride of 2 is applied, generating 192 × 128 feature maps.

8) Follows another convolution with 192 kernels with a kernel size of 4 and a stride of 4 replacing both Max-Pooling and ReLU layer, producing 192 × 32 maps.

9) Then, the feature maps are flattened, obtaining 6144 values, and a fully connected (FC) layer of 6144 neurons is applied, leaving the number of values unaltered. This layer is not trained during the first phase of the training.

10) The second FC layer is the last layer of the network generating the output.

The network infers an estimate of the net number of counts for 58 XRF spectral series, of which 38 are summarized in table S2, and additional 20 XRF single emission lines are listed in table S3. Once the network is trained, we add a Softplus layer at the end of the network and train again. This further increases the accuracy of the network and removes negative counts.

Synthetic training dataset

We consider two relevant ways to build the training datasets. The first one consists of the use of experimental data, i.e., datasets of already analyzed paintings, while the second way consists of generating an artificial synthetic dataset. While building the training datasets with experimental data is feasible, we find it challenging for several reasons. First, the composition of the dataset is dependent on the analyzed paintings or mockups. This readily becomes a limiting factor as the model cannot be trained to predict elements not previously measured, and any extensions of these datasets can present noteworthy challenges as these data are not only sample dependent. They are also instrumentation specific. In addition, the resulting datasets are not balanced, there are chemical elements that are present often, e.g., white lead used in the preparatory layer, while others can be found only in later repainting, and restoration materials that can vary wildly even regarding artworks from the same period that otherwise have similar compositions. Another issue is that these datasets often come with systematic errors. These systematic errors are likely to vary for different analyzed paintings. Each scan has its own setup, both experimental and the settings used for the analysis. While this, in general, will not affect on the actual analysis of the elemental maps, it can lead to hindering of the training, resulting in suboptimal performance and inability to correctly predict the intensities. Alternatively, one can use synthetic datasets to train the networks. Given that one can generate reasonable synthetic spectra, this offers many benefits. Mainly, (i) each spectrum has associated known labels; (ii) we obtain convoluted spectra without Poisson noise; (iii) it can be expanded easily with respect to the experimental one, introducing any combination of elements if needed. Last, the spectra are not dependent on a set of paintings and balancing.

The synthetic dataset generated for our model is based on simulations covering combinations of all the chemical elements needed. We have used XMI-MSIM software that is an open-source tool designed for predicting XRF spectra using MC simulations (*22*). It allows the user to customize the elemental composition of the dataset by using real scanning configurations. The synthetic XRF spectra are generated using MC simulations based on a fundamental parameters approach and tuned for the geometry and the x-ray source of our MA-XRF setup. In the case presented here, we have used a Rh-anode x-ray source coupled with a polycapillary. To reproduce the experimental spectral distribution of the source, the transmission function of the optic and the following emission spectrum are calculated semi-empirically using Compton scattering of a Mylar standard. The most challenging step here is to estimate the transmission function. However, this step only must be done once for the given optics. Once the excitation source is well defined, it is possible to reproduce the experimental XRF spectra with high fidelity. The one drawback of the calculation is that diffraction peaks modeling are not included in the MC simulations. This remains a limitation in XRF analysis, affecting even traditional deconvolution methods.

We show the comparison of synthetic and experimental spectra for a geological calcite in Fig. 2A. To create the synthetic dataset, we model the paintings using a five-layer model as depicted in Fig. 1A. At the bottom, we place a gypsum support followed by a preparation layer. The preparation layer is modeled as a white lead pigment mixed with linseed oil as a binder. We set the thickness of the preparation layer to 60 μm. Next is the pictorial layer that we model as a mixture of pigments and a binder. We keep a fixed volume ratio of pigments/binder 1:1. We use volume fractions rather than the mass fractions to better account for varying densities of the pigments. The pigments are chosen randomly from a list of 57 pigments. Both historical and modern pigments are included (see table S1). The number of pigments in the layer is not fixed and instead is taken from a Poisson distribution. On average, two pigments are selected. The thickness of the pictorial layer is chosen randomly from a uniform distribution ranging from 1 to 120 μm. On top, we add a layer of varnish. The last layer models the air path corresponding to the space between the sample and the x-ray source.

In Fig. 2B, we show a simulated spectrum compared with an experimental spectrum from the MA-XRF dataset of the *Virgin Mary* panel. This is to demonstrate that we reliably reproduce the experimental spectra including the background. In addition to the above physical model of the painting, we also generate a dataset without the hydrocerussite layer to model spectra where we do not measure any lead (see fig. S6). The main goal of this exercise is to construct a dataset that appropriately represents any typical 15th century painting. Ideally, the space covered by the synthetic dataset is larger than the union of all the relevant experimental datasets. This is to guarantee that the solutions of the network are not based on extrapolation but rather on interpolation. We generated a synthetic dataset of 500,000 random spectra following the procedure described above. We make a great deal of effort to make sure that the synthetic dataset is as representative as possible. Figure 9 displays the logarithms of 2D distributions, i.e., the projections of *n*-dimensional elemental maps to show that we indeed cover the experimental datasets. We divided by the counts of Pb-L to make the distributions scale invariant.

Experimental dataset

The experimental datasets used for validating our AI/ML model were obtained through in-situ MA-XRF investigations of Raphael's artworks at the Museo e Real Bosco di Capodimonte in Napoli. Specifically, we show the MA-XRF datasets of the panels, *God the Father* and head of *Virgin Mary*, which are fragments of the Baronci Altarpiece painted by Raphel in 1500–1501 (see fig. S1). Two distinct MA-XRF setups, both developed at the XRAYLab of

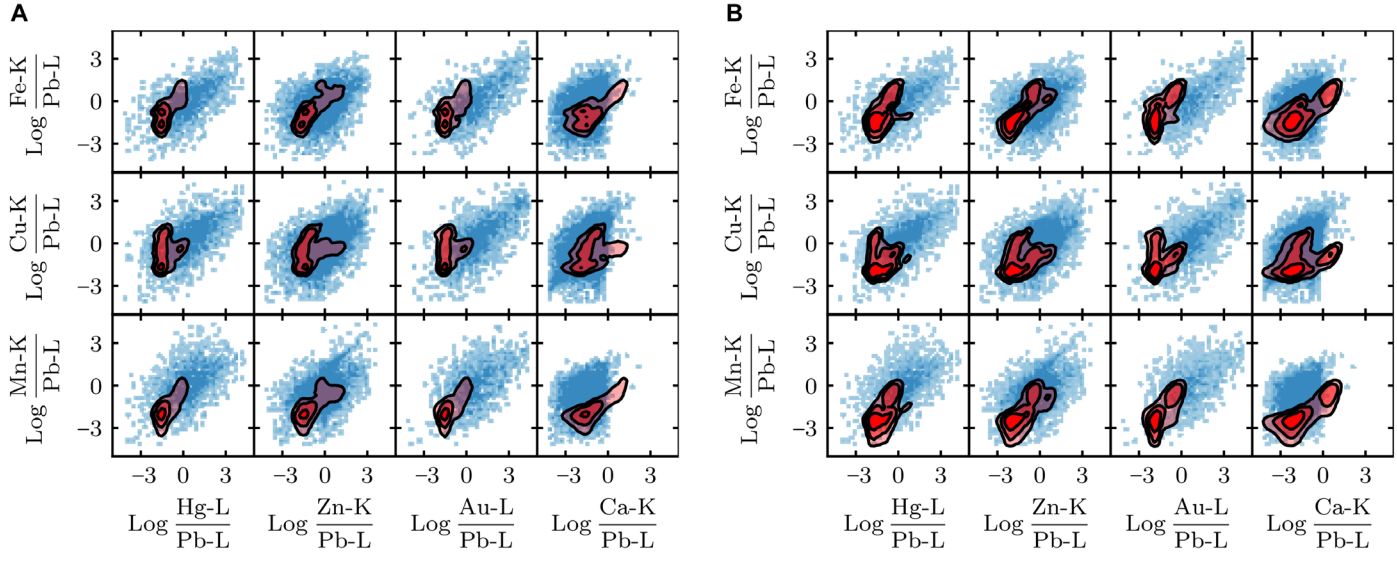

Fig. 9. Synthetic spectra datasets. We show logarithms of ratios of selected elemental lines and corresponding net counts of Pb-L. The blue 2D histograms in the background represent the spectra of the synthetic datasets used. The red contours indicate the experimental spectra. All net counts are normalized by Pb-L to make them independent to the change of scale. The graphs show that the synthetic spectra cover the space where we expect the experimental datasets. The experimental datasets correspond to the net counts estimated using the deconvolution. (**A**) Experimental datasets of MA-XRF of the *Virgin Mary*. (**B**) Experimental dataset of the micro-XRF of the detail of the *God the Father*.

ISPC-CNR in Catania, were used across different scanning sessions. The first setup, used for scanning the entire panels, comprises an Rh anode source, focused with a polycapillary, and a detection system with two silicon drift detectors (SDDs) (*15*). The second setup, used for the high-resolution acquisitions, features a 3D array of six SDDs (*30*). The dataset of the panel *God the Father* was taken at a 1-mm scanning step and 12-ms dwell time per pixel and consists of 1.1 M pixels; the dataset of the panel head of the *Virgin Mary* was taken at a step size of 1 mm and 12-ms dwell-time per pixel and consists of 210,000 pixels. The close-up on the *God the Father* was taken at a step size of 250 μm and 5-ms dwell time and consists of 1.2 M pixels. The high-resolution details of the *Virgin Mary* were taken at a step size of 50 μm and 10 ms and consist of 340,000 pixels.

Supplementary Materials

This PDF file includes:

Supplementary Text
Figs. S1 to S9
Tables S1 to S5

REFERENCES AND NOTES

1. J. K. Delaney, K. A. Dooley, A. van Loon, A. Vandivere, Mapping the pigment distribution of Vermeer's girl with a pearl earring. *Herit. Sci.* **8**, 4 (2020).
2. F. Gabrieli, K. A. Dooley, M. Facini, J. K. Delaney, Near-UV to mid-IR reflectance imaging spectroscopy of paintings on the macroscale. *Sci. Adv.* **5**, eaaw7794 (2019).
3. N. De Keyser, F. Broers, F. Vanmeert, S. De Meyer, F. Gabrielli, E. Hermens, G. Van der Snickt, K. Janssens, K. Keune, Reviving degraded colors of yellow flowers in 17th century still life paintings with macro- and microscale chemical imaging. *Sci. Adv.* **8**, eabn6344 (2022).
4. S. De Meyer, F. Vanmeert, R. Vertongen, A. Van Loon, V. Gonzalez, J. Delaney, K. Dooley, J. Dik, G. Van der Snickt, A. Vandivere, K. Janssens, Macroscopic x-ray powder diffraction imaging reveals Vermer's discriminating use of lead white pigments in *Girl with a Pearl Earring*. *Sci. Adv.* **5**, eaax1975 (2019).
5. C. Miliani, L. Monico, M. J. Melo, S. Fantacci, E. M. Angelin, A. Romani, K. Janssens, Photochemistry of artists' dyes and pigments: Towards better understanding and prevention of colour change in works of art. *Angew. Chem. Int. Ed. Engl.* **57**, 7324–7334 (2018).
6. K. A. Dooley, D. M. Conover, L. D. Glinsman, J. K. Delaney, Complementary standoff chemical imaging to map and identify artist materials in an early Italian renaissance panel painting. *Angew. Chem. Int. Ed. Engl.* **126**, 13995–13999 (2014).
7. L. Monico, L. Cartechini, F. Rosi, A. Chieli, C. Grazia, S. De Meyer, G. Nuyts, F. Vanmeert, K. Janssens, M. Cotte, W. De Nolf, G. Falkenberg, I. C. A. Sandu, E. S. Tveit, J. Mass, R. P. de Freitas, A. Romani, C. Miliani, Probing the chemistry of CdS paints in *The Scream* by in situ noninvasive spectroscopies and synchrotron radiation x-ray techniques. *Sci. Adv.* **6**, eaay3514 (2020).
8. A. van Loon, P. Noble, D. de Man, M. Alfeld, T. Callewaert, G. Van der Snickt, K. Janssens, J. Dik, The role of smalt in complex pigment mixtures in Rembrandt's Homer 1663: Combining MA-XRF imaging, microanalysis, paint reconstructions and OCT. *Herit. Sci.* **8**, 90 (2020).
9. Z. Sabetsarvestani, B. Sober, C. Higgitt, I. Daubechies, M. R. D. Rodrigues, Artificial intelligence for art investigation: Meeting the challenge of separating x-ray images of the *Ghent Altarpiece*. *Sci. Adv.* **5**, eaaw7416 (2019).
10. T. Kleynhans, C. M. S. Patterson, K. A. Dooley, D. W. Messinger, J. K. Delaney, An alternative approach to mapping pigments in paintings with hyperspectral reflectance image cubes using artificial intelligence. *Herit. Sci.* **8**, 84 (2020).
11. S. Kogou, L. Lee, G. Shahtahmassebi, H. Liang, A new approach to the interpretation of XRF spectral imaging data using neural networks. *X-Ray Spectrom.* **50**, 310–319 (2021).
12. S. Kogou, G. Shahtahmassebi, A. Lucian, H. Liang, B. Shui, W. Zhang, B. Su, S. Van Schaik, From remote sensing and machine learning to the history of the silk road: Large scale material identification on wall paintings. *Sci. Rep.* **10**, 19312 (2020).
13. M. Vermeulen, A. M. Geachy, B. Xu, H. Chopp, A. Katsaggelos, R. Meyers, M. Alfeld, M. Walton, Xrfast a new software package for processing of Ma-XRF datasets using machine learning. *J. Anal. At. Spectrom* **37**, 2130–2143 (2022).
14. M. Alfeld, W. De Nolf, S. Cagno, K. Appel, D. P. Siddons, A. Kuczewski, K. Janssens, J. Dik, K. Trentelman, M. Walton, A. Sartorius, Revealing hidden paint layers in oil paintings by means of scanning macro-XRF: A mock-up study based on rembrandt's "An old man in military costume". *J. Anal. At. Spectrom* **28**, 40–51 (2013).
15. F. P. Romano, C. Caliri, P. Nicotra, S. Di Martino, L. Pappalardo, F. Rizzo, H. C. Santos, Real-time elemental imaging of large dimension paintings with a novel mobile macro x-ray fluorescence (MA-XRF) scanning technique. *J. Anal. At. Spectrom* **32**, 773–781 (2017).
16. A. T. da Silva, S. Legrand, G. Van der Snickt, R. Featherstone, K. Janssens, G. Bottinelli, MA-XRF imaging on Renè Magritte's La *condition humaine*: Insights into the artist's palette and technique and the discovery of a third quarter of *La pose enchantèe*. *Herit. Sci.* **5**, 37 (2017).
17. G. Van der Snickt, S. Legrand, I. Slama, E. Van Zuien, G. Gruber, K. Van der Stighelen, L. Klaassen, E. Oberthaler, K. Janssens, In situ macro x-ray fluorescence (MA-XRF) scanning as a non-invasive tool to probe for subsurface modifications in paintings by P.P. Rubens. *Microchem. J.* **138**, 238–245 (2018).
18. K. A. Dooley, E. M. Gifford, A. van Loon, P. Noble, J. G. Zeibel, D. M. Conover, M. Alfeld, G. Van der Snickt, S. Legrand, K. Janssens, J. Dik, J. K. Delaney, Separating two painting campaigns in *Saul and David*, attributed to Rembrandt, using macroscale reflectance and XRF imaging spectroscopies and microscale paint analysis. *Herit. Sci.* **6**, 46 (2018).
19. V. A. Solè, E. Papillon, M. Cotte, P. Walter, J. Susini, A multiplatform code for the analysis of energy-dispersive X-ray fluorescence spectra. *Spectrochim. Acta Part B. At. Spectrosc.* **62**, 63–68 (2017).
20. M. Alfeld, K. Janssens, Strategies for processing mega-pixel X-ray fluorescence hyperspectral data: A case study on a version of Caravaggio's painting Supper at Emmaus. *J. Anal. At. Spectrom* **30**, 777–789 (2015).
21. B. Vekemans, K. Janssens, L. Vincze, F. Adams, P. Van Espen, Analysis of x-ray spectra by iterative least squares (AXIL): New developments. *X-Ray Spectrom.* **23**, 278–285 (1994).
22. H. C. Santos, C. Caliri, L. Pappalardo, R. Catalano, A. Orlando, F. Rizzo, F. P. Romano, Identification of forgeries in historical enamels by combining the non-destructive scanning XRF imaging and alpha-PIXE portable techniques. *Microchem. J.* **124**, 241–246 (2016).
23. M. Vermeulen, L. Burgio, N. Vandeperre, E. Driscoll, M. Viljoen, J. Woo, M. Leona, Beyond the connoisseurship approach: Creating a chronology in Hokusai prints using non-invasive techniques and multivariate data analysis. *Herit. Sci.* **8**, 62 (2020).
24. M. Vermeulen, K. Smith, K. Eremin, G. Rayner, M. Walton, Application of uniform manifold approximation and projection (UMAP) in spectral imaging of artworks. *Spectrochim. Acta A Mol. Biomol. Spectrosc.* **252**, 119547 (2021).
25. E. Pouyet, N. Rohani, A. K. Katsaggelos, O. Cossairt, M. Walton, Innovative data reduction and visualization strategy for hyperspectral imaging datasets using t-SNE approach. *Pure Appl. Chem.* **90**, 493–506 (2018).
26. M. Alfeld, S. Pedetti, P. Martinez, P. Walter, Joint data treatment for VIS–NIR reflectance imaging spectroscopy and XRF imaging acquired in the Theban necropolis in Egypt by data fusion and t-SNE. *C. R. Phys.* **19**, 625–635 (2018).
27. C. Jones, N. S. Daly, C. Higgitt, M. R. D. Rodrigues, Neural network-based classification of x-ray fluorescence spectra of artists' pigments: An approach leveraging a synthetic dataset created using the fundamental parameters method. *Herit. Sci.* **10**, 88 (2022).
28. B. J. Xu, Y. Wu, P. Hao, M. Vermeulen, A. McGeachy, K. Smith, K. Eremin, G. Rayner, G. Verri, F. Willomitzer, M. Alfeld, J. Tumblin, A. Katsaggelos, M. Walton, Can deep learning assist automatic identification of layered pigments from XRF data? *J. Anal. At. Spectrom.* **37**, 2672–2682 (2022).
29. T. Schoonjans, L. Vincze, V. A. Solé, M. Sanchez del Rio, P. Brondeel, G. Silversmit, K. Appel, C. Ferrero, A general Monte Carlo simulation of energy dispersive X-ray fluorescence spectrometers—Part 5: Polarized radiation, stratified samples, cascade effects, M-lines. *Spectrochim. Acta Part B At. Spectrosc.* **70**, 10–23 (2012).
30. F. P. Romano, E. Puglia, C. Caliri, D. P. Pavone, M. Alessandrelli, A. Busacca, C. G. Fatuzzo, K. J. Fleischer, C. Pernigotti, Z. Preisler, C. Vassallo, G. Verhasselt, C. Miliani, G. Ranocchia, Layout of ancient Greek papyri through lead-drawn ruling lines revealed by macro x-ray fluorescence imaging. *Sci. Rep.* **13**, 6582 (2023).
31. A. Roy, M. Spring, C. Plazzotta, Raphael's early work in the national gallery: Paintings before Rome. *Natl. Gall. Tech. Bull.* **25**, 4–35 (2004).
32. C. Higgitt, R. White, Analyses of paint media: New studies of Italian painting of the fifteenth and sixteenth centuries. *Natl. Gall. Tech. Bull.* **26**, 88–97 (2005).
33. M. Spring, Raphael's materials: Some new discoveries and their context within early sixteenth-century painting. in *Raphael's painting technique: Working practices before Rome*, A. Roy, M. Spring, Eds. (National Gallery, London, 2007) pp. 77–86.
34. A. Cerasuolo, Raffaello a Capodimonte: Dall'inizio alla piena maturità, in *Raffaello. L'officina dell'artista*, A. Cerasuolo, A. Zezza, Eds. (Editori Paparo, 2021), pp. 80–99.
35. C. Ricci, I. Borgia, B. G. Brunetti, C. Miliani, A. Sgamellotti, C. Seccaroni, P. Passalacqua, The Perugino's palette: Integration of an extended in situ XRF study by Raman spectroscopy. *J. Raman Spectrosc.* **35**, 616–621 (2004).

Acknowledgments: We wish to thank the Museo e Real Bosco di Capodimonte (Napoli) and its director for having granted permission to perform the MA-XRF scanning of the Raphael paintings discussed in this research. We wish to thank A. Zezza, A. Cerasuolo, and M. Cardinali for having assisted us in the experimental work performed on the paintings and for

enlightening discussion on the pigment materials used by Raphael, his executive process, and modus operandi. We thank the Laboratori Nazionali del Sud of INFN in Catania for the infrastructural support. **Funding:** This work was financially supported by the H2IOSC "Humanities and Cultural Heritage Italian Open Science Cloud", IR0000029, CUP B63C22000730005, NRP M4C2, Investment 3.1, Funded by the European Union—NextGenerationEU; the CHANGES, SPOKE 5 "Science and Technologies for Sustainable Diagnostics of Cultural Heritage," PE 0000020, CUP B53C22003890006, NRP M4C2 Investment 1.3, funded by the European Union—NextGenerationEU; the SAMOTHRACE, "Sicilian MicronanoTech Research And Innovation Center," ECS 00000022, CUP B63C22000620005, NRP M4C2 Investment 1.5, funded by the European Union—NextGenerationEU; and the E-RIHS.it Italian national node of the European Infrastructure of Heritage Science (E-RIHS) funded by the European Commission, H2020-INFRADEV-2016-2, GA 739503. **Author contributions:** Conceptualization: Z.P. and F.P.R. Methodology: Z.P. Investigation: Z.P., R.A., A.B., and C.C. Visualization: Z.P. and F.P.R. Supervision: F.P.R. and C.M. Writing—original draft: Z.P. and F.P.R. Writing—review and editing: Z.P., C.C., C.M., and F.P.R. **Competing interests:** The authors declare that they have no competing interests. **Data and materials availability:** All data needed to evaluate the conclusions in the paper are present in the paper and/or the Supplementary Materials. The data for this study have been deposited in Zenodo (https://zenodo.org/records/12583799).

Submitted 3 April 2024
Accepted 19 August 2024
Published 25 September 2024
10.1126/sciadv.adp6234